OCEANOGRAPHY

Reduced nitrite accumulation at the primary nitrite maximum in the cyclonic eddies in the western North Pacific subtropical gyre

Li Liu[1], Mingming Chen[1], Xianhui S. Wan[1,2], Chuanjun Du[3], Zhiyu Liu[1], Zhendong Hu[1], Zong-Pei Jiang[4], Kuanbo Zhou[1], Hongyang Lin[1], Hui Shen[1], Duo Zhao[1], Lanying Yuan[1], Lei Hou[1], Jin-Yu T. Yang[1], Xiaolin Li[1], Shuh-Ji Kao[1], Emily J. Zakem[5], Wei Qin[6], Minhan Dai[1], Yao Zhang[1]*

Nitrite, an intermediate product of the oxidation of ammonia to nitrate (nitrification), accumulates in upper oceans, forming the primary nitrite maximum (PNM). Nitrite concentrations in the PNM are relatively low in the western North Pacific subtropical gyre (wNPSG), where eddies are frequent and intense. To explain these low nitrite concentrations, we investigated nitrification in cyclonic eddies in the wNPSG. We detected relatively low half-saturation constants (i.e., high substrate affinities) for ammonia and nitrite oxidation at 150 to 200 meter water depth. Eddy-induced displacement of high-affinity nitrifiers and increased substrate supply enhanced ammonia and nitrite oxidation, depleting ambient substrate concentrations in the euphotic zone. Nitrite oxidation is more strongly enhanced by the cyclonic eddies than ammonia oxidation, reducing concentrations and accelerating the turnover of nitrite in the PNM. These findings demonstrate a spatial decoupling of the two steps of nitrification in response to mesoscale processes and provide insights into physical-ecological controls on the PNM.

INTRODUCTION

Nitrogen cycling plays a major role in marine and global primary production and carbon cycling. As a key intermediate, nitrite (NO_2^-) is involved in multiple biologically mediated redox processes, and NO_2^- concentrations have been used as an indicator for the homeostasis of oxidative and reductive pathways in the marine nitrogen cycle (*1*). It is well-known that NO_2^- has a commonly observed unimodal vertical profile in oxygenated, stratified waters with a peak near the bottom of the euphotic zone, known as the primary nitrite maximum (PNM) (*2*). The evidence indicates that ammonia (NH_3) oxidation [here, defined as the total NH_3 and ammonium (NH_4^+) oxidized to NO_2^-], performed by ammonia-oxidizing archaea (AOA) and bacteria (AOB), is the primary source of NO_2^- in the PNM, while NO_2^--oxidizing bacteria (NOB) are responsible for its oxidation to nitrate (NO_3^-), representing the primary sink for NO_2^- (*3*–*8*). A population dynamics model developed by Zakem *et al.* (*9*) suggests that the higher accumulation of NO_2^- than NH_4^+ at the PNM reflects different subsistence resource concentrations of NH_3 and NO_2^- for AOA and NOB, respectively, which are set by the traits of the microorganisms (*10*). Although the excretion of NO_2^- from the incomplete assimilatory reduction of NO_3^- by phytoplankton may be another source of NO_2^- in the PNM in some locations (*11*), the current understanding is that the two steps of nitrification (NH_3 and NO_2^- oxidation as source and sink, respectively) principally determine NO_2^- accumulation at the PNM in the oligotrophic open ocean. These two steps also modulate the speciation of dissolved inorganic nitrogen, which ultimately limits primary production (*12*, *13*).

Notably, both global ocean modeling (*9*) and field research (*14*, *15*) have indicated higher maximum NO_2^- concentrations in high latitudes and equatorial upwelling regions and the lowest NO_2^- concentrations in the subtropical gyres, forming a unique meridional distribution pattern in the upper ocean. The global ocean biogeochemical model that resolves dynamic AOA and NOB populations captures this pattern by assuming a tight coupling between the oxidation rates of NH_3 and NO_2^-, suggesting that the steady-state concentrations of NO_2^- may vary across the ocean despite this coupling (*9*, *16*). The positive correlation between nitrification rates and NO_2^- concentrations at the PNM in the model further suggests that variables controlling the subsistence resource concentrations of AOA and NOB, such as the population's maximum growth rate, loss rate, and substrate affinity, vary with nitrification rates across the ocean. Although the oxidation rates of NH_3 and NO_2^- are often tightly coupled, they can become decoupled in certain oceanic regions, particularly in the presence of active physical dynamic processes such as eddies. Therefore, a deviation from a steady state due to mesoscale (eddy) circulation should contribute to spatial and temporal heterogeneity in the basin-scale patterns, which is not resolved in the global model. Therefore, understanding how different components of the nitrification system change with mesoscale dynamic processes and the mechanisms that control the decoupling between NH_3 and NO_2^- oxidation is crucial for accurately modeling and predicting the natural variability of PNM in the open ocean. This variability has important implications for the balance between reduced and oxidized nitrogen pools, which, in turn, can affect the availability of nitrogen for biological productivity. These insights can improve our understanding of the nitrogen cycle's homeostatic regulation and its response to changing environmental conditions.

[1]State Key Laboratory of Marine Environmental Science and College of Ocean and Earth Sciences, Xiamen University, Xiamen, China. [2]Department of Geosciences, Princeton University, Princeton, NJ, USA. [3]State Key Laboratory of Marine Resource Utilization in South China Sea, Hainan University, Haikou, China. [4]Ocean College, Zhejiang University, Zhoushan, China. [5]Department of Global Ecology, Carnegie Institution for Science, Stanford, CA, USA. [6]Department of Microbiology and Plant Biology, University of Oklahoma, Norman, OK, USA.
*Corresponding author. Email: yaozhang@xmu.edu.cn

The western North Pacific subtropical gyre (wNPSG) is an "ocean desert" region (*17*) with one of the lowest concentrations of NO_2^- among the global PNM. Because of baroclinically unstable countercurrents, the wNPSG is also one of the most active mesoscale eddy regions in the global ocean (*18*–*20*). Mesoscale eddies, including cold-core cyclonic eddies and warm-core anticyclonic eddies, exert notable impacts on biogeochemical processes, such as primary production, organic matter remineralization, and oxygen consumption, through the transport and redistribution of material and energy (*20*, *21*). We hypothesize that these frequent and intense mesoscale dynamic events may also affect nitrification by changing the coupled relationship between NH_3 and NO_2^- oxidation and, consequently, influencing the magnitude of the PNM. Because nitrification converts reduced nitrogen into oxidized forms, the formation of a nitrification-dependent PNM with very low NO_2^- concentrations in the wNPSG indicates maximum possible production of NO_3^- from regenerated reduced nitrogen, which may have an impact on the estimates of new primary production (measured by NO_3^- uptake) and carbon export from the euphotic zone. To test the hypothesis that mesoscale processes affect nitrification dynamics, we conducted the first study involving mesoscale eddy tracking in the wNPSG, combining NH_3 and NO_2^- oxidation rates and kinetics measurements with key genetic analyses. Here, our comprehensive survey of nitrification throughout two cyclonic eddies suggests that mesoscale processes do play an important role in shaping the distribution pattern of the PNM in the dynamic ocean.

RESULTS

Eddy-induced changes in hydrography, nutrients, and chlorophyll

Among a number of mesoscale eddies occurring in the wNPSG, we tracked two cyclonic eddies (E1 and E2) during a research cruise, where a total of 17 sites were sampled for nitrification analyses (Fig. 1, A and B). According to sea level anomaly (SLA) observations from satellite altimetry, sea surface heights (SSHs) of the two eddies were lower than the surrounding waters and gradually moved westward during the cruise (Fig. 1B). There were clearly shoaled depths of low temperature, high salinity, high fluorescence values (mainly from chlorophyll), and relatively low oxygen concentrations in the upper 200 m (Fig. 1, C to F), accompanied by the lowered SSH in the eddy centers (Fig. 1, A and B). The temperature above 250 m in the eddy centers (SLA ≤ -0.05 m) and edges ranged from 16.9°C to 27.8°C and 17.5°C to 28.2°C, respectively (Fig. 1C). The depth of the deep chlorophyll maximum (DCM) varied from 86 to 162 m across all investigated sites. The average depth of the DCM in the eddy centers and edges was 107 and 139 m, respectively, where the average (±SD; hereafter, applied to averages from this study) fluorescence values were 0.53 ± 0.12 and 0.44 ± 0.09 μg liter^{-1}, respectively (Fig. 1E). Oxygen concentrations indicated the investigated eddy systems contained fully oxygenated waters (Fig. 1F).

NH_4^+ concentrations were consistently low within the upper 500 m across all sites, ranging from below the detection limit to 17 nM. Nevertheless, NH_4^+ concentrations at the eddy center were significantly lower than that at the edge sites (Mann-Whitney *U* test, $P < 0.01$; Fig. 2A), with the average concentration at every depth ranging from 1.1 to 8.4 nM (center) and 5.4 to 11.1 nM (edge). NO_2^- concentrations exhibited a wider range than NH_4^+, varying from 5.9 to 95.6 nM and from 3.3 to 134.9 nM at the center and edge sites, respectively. The typical PNM (i.e., near the bottom of the euphotic zone) was observed at all sites (Fig. 2B). Notably, there was a clear shoaling (80 to 140 m, average 115 m) and decreased magnitude (22.3 to 95.6 nM) of the PNM at the eddy center compared with the edge sites (120 to 150 m; average, 137 m; 35.9 to 134.8 nM), as confirmed by the single-peak fitting curve ($P < 0.001$) for NO_2^- concentrations against depth (Fig. 2B). NO_3^- was depleted (below the detection limit to 82.9 nM) in the surface water of all sites. However, the depth of the nitracline, defined as the depth of 0.1 μM NO_3^- (*22*), at the eddy center (average, 102 m) was significantly shallower than the edge (average, 139 m; $P < 0.01$; Fig. 2C).

NH_3 and NO_2^- oxidation rates and kinetics

The depth profiles of the NH_3 and NO_2^- oxidation rates (Fig. 3, A and B) showed a similar vertical distribution pattern with low or undetectable rates in the surface waters and increasing with depth to a subsurface maximum around the base of the euphotic zone. The rates then decreased strongly with increasing depth. In the upper 500 m, the rates of NH_3 oxidation and NO_2^- oxidation were significantly higher at the eddy center (below detection to 7.47 and 11.29 nM day^{-1}, respectively) than the edge sites (below detection to 4.33 and 3.14 nM day^{-1} for NH_3 oxidation and NO_2^- oxidation, respectively; $P < 0.05$). Water depths of the maximal NH_3 and NO_2^- oxidation rates were much shallower at the eddy center sites (120 and 140 m, respectively; Fig. 3A) than at the edge sites (180 and 200 m, respectively; Fig. 3B). Likewise, the average depth of the euphotic zone [defined as 0.1% of surface photosynthetically active radiation (PAR)] was shallower in the eddy center (148 m) compared to that in the edge (163 m; right plot in Fig. 3B). On the basis of the depth-integrated rates in the euphotic zone (upper 150 m, no data between 150 and 163 m), the average increase in NO_2^- oxidation rate (357.6 ± 16.9%) between the eddy center and edge was greater than the increase in NH_3 oxidation rate (132.1 ± 9.7%). When calculating the depth integration of the upper 200 m (the deepest rate maximum), the average increases in NO_2^- and NH_3 oxidation rates were 197.4 ± 9.3% and 75.4 ± 5.3%, respectively.

The principal components analysis (PCA) of eddy-induced physical and biogeochemical gradients and nitrification rates revealed well-separated clusters of eddy center and edge sites; the center sites were characterized by negative SLA, shoaling of the nitracline and DCM depth, enhanced NH_3 and NO_2^- oxidation, and low NO_2^- concentrations at the PNM (Fig. 4A). The PCA of each depth sample demonstrated the largest variations in NH_4^+ and NO_2^- concentrations, fluorescence, and nitrification rates between 90 and 200 m of the eddy center (Fig. 4B), indicating that the cyclonic eddy induced strong responses around the base of the euphotic zone.

The kinetics of NH_3 and NO_2^- oxidation were analyzed at the eddy center sites P16_2 and P17 (Fig. 1). The dependence of the NH_3 and NO_2^- oxidation rates on the substrates followed Michaelis-Menten (M-M) kinetics at all investigated depths (100, 150, and 200 m; Fig. 5, A to D). Both the potential maximum rate (V_{max}, 2.1 to 6.2 nM day^{-1}) and the half-saturation constant (K_s, 8 to 43.6 nM) of NH_3 oxidation (Fig. 5, A and B) were significantly lower than the V_{max} (8.9 to 18.4 nM day^{-1}) and K_s (64.8 to 124.5 nM) of NO_2^- oxidation (Fig. 5, C and D; $P < 0.05$). The substrate-specific affinity

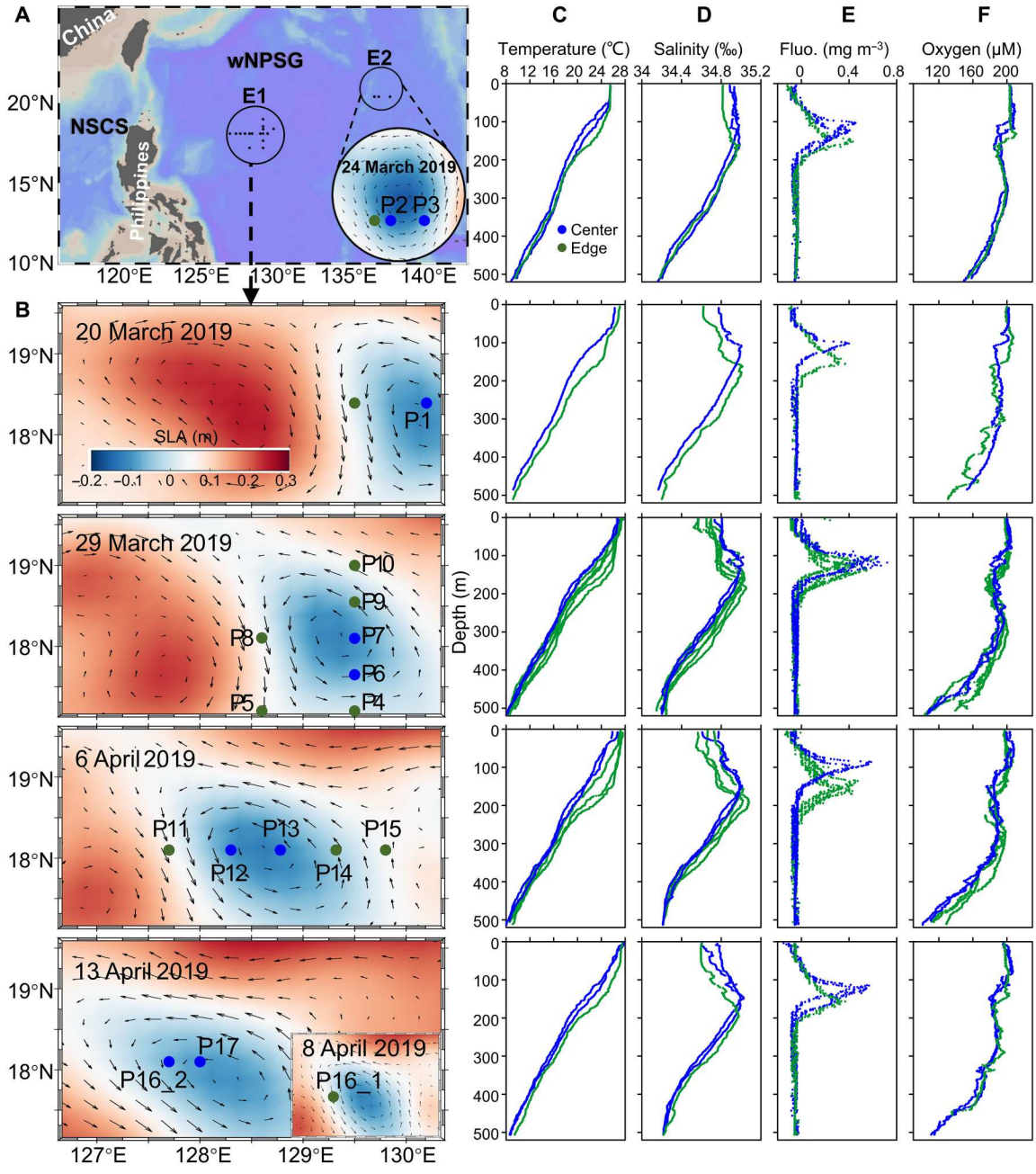

Fig. 1. Study area, sampling sites, sea level anomaly (SLA), as well as the hydrological parameters and fluorescence distribution in the upper 500 m water depth. (**A**) Sampling sites in two cyclonic eddies (E1 and E2). The background of E2 is a real-time sea surface height altimetry (or SLA), remotely sensed image with geostrophic currents (meters per second) from the Copernicus Marine Environmental Monitoring Service (http://marine.copernicus.eu) for 24 March 2019. NSCS, Northern South China Sea. (**B**) Sampling sites of E1 in the background of the SLA map with roughly corresponding sampling time. (**C**) Temperature, (**D**) salinity, (**E**) fluorescence, and (**F**) oxygen concentrations were obtained from conductivity-temperature-depth casts. The blue dots represent the eddy centers; the green dots represent the edges.

was further estimated as $a° = V_{max}/K_s$, and a relatively higher $a°$ of marine AOA (0.26 to 0.75 day^{-1}) than that of NOB (0.10 to 0.21 day^{-1}) was observed at 150 and 200 m ($P < 0.05$). Vertically, the K_s values of NH_3 and NO_2^- oxidation generally decreased, while the $a°$ values increased from 100 to 200 m. These changes suggest that nitrifiers had an increased affinity at depths where nutrients were much more depleted.

Abundance and distribution of AOA and NOB

The archaeal *amoA* gene abundance in the upper 500 m ranged from 36 to 2.84 × 10^6 copies $liter^{-1}$ and from 43 to 1.74 × 10^6 copies $liter^{-1}$ at the eddy center and edge sites, respectively. The *Nitrospina* 16*S* ribosomal RNA (rRNA) gene abundance at the eddy center and edge sites varied from 36 to 5.56 × 10^5 copies $liter^{-1}$ and from 51 to 1.92 × 10^5 copies $liter^{-1}$, respectively (Fig. 3, C and D). Although the comparison between a functional gene and a specific

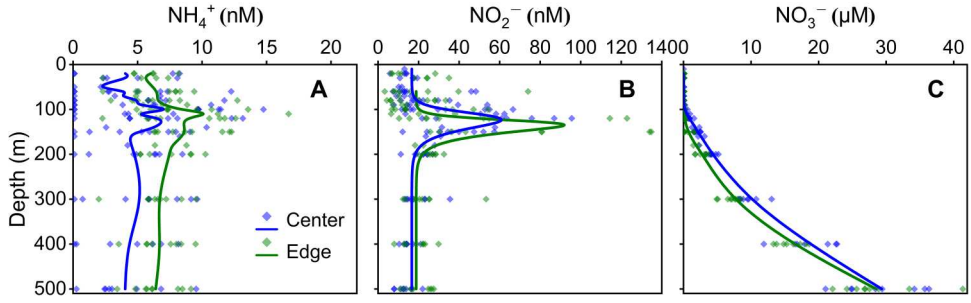

Fig. 2. Dissolved inorganic nitrogen distributions in the upper 500 m water depth at all sampling sites. (**A**) NH_4^+ concentrations; (**B**) NO_2^- concentrations; (**C**) NO_3^- concentrations. The blue and green diamonds represent the eddy centers and edges, respectively. In (A) and (C), lines represent B-spline curves that display the average concentration at every depth in the eddy centers (blue) and edges (green). Lines in (B) denote the single-peak fitting curve via the asymmetric double sigmoidal (Asym2Sig) function for NO_2^- concentration against depth in the eddy centers (blue; $R^2 = 0.504$, $P < 0.01$ for 10 to 500 m) and edges (green; $R^2 = 0.382$, $P < 0.01$ for 60 to 500 m).

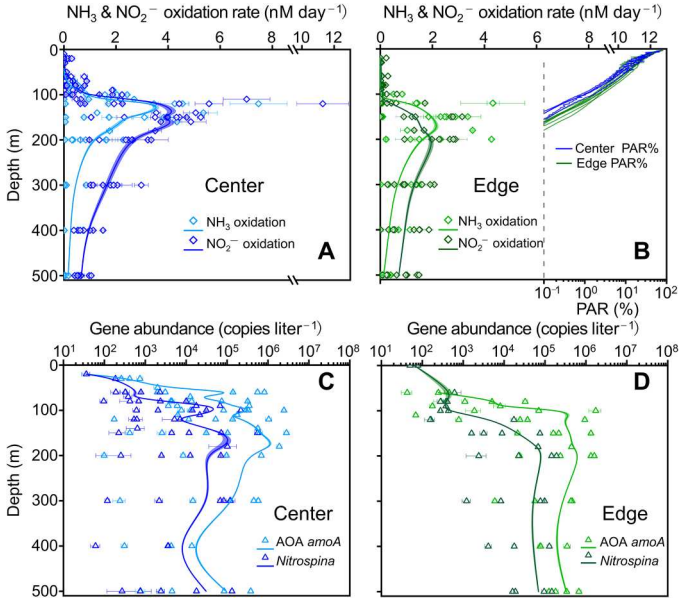

Fig. 3. Vertical distribution of nitrification rates and nitrifier gene abundances. NH_3 and NO_2^- oxidation rates in the (**A**) eddy center and (**B**) edge. AOA *amoA* and *Nitrospina* 16*S* ribosomal RNA (rRNA) gene abundances in the (**C**) eddy center and (**D**) edge. Rates were derived from the slope of the linear regression of four independent time-course incubation experiments. The error bars for the rates indicate the SD of the replicates. The error bars for gene abundances represent the SD of three technical replicates. Some error bars are not visible because they are smaller than the symbols. Lines denote the average oxidation rates or gene abundances based on all sampling sites. The shaded area represents the propagated error from the SEs.

16*S* rRNA gene may have limitations, we can infer from our results that the abundance of AOA was significantly higher than that of the NOB *Nitrospina* ($P < 0.01$). Along a depth gradient, there was an abundance jump in archaeal *amoA* (defined as 10^4 copies liter^{-1}) and *Nitrospina* 16*S* rRNA genes (defined as 10^3 copies liter^{-1}), where their abundance suddenly increased from very low at surface depths to more abundant in deeper ocean layers. The depths of this abundance jump were shallower at the eddy center sites (60 to 100 m for both genes) compared to that at the edge sites (80 to 150 m for archaeal *amoA* gene and 120 to 150 m for *Nitrospina* 16*S* rRNA gene; $P < 0.05$ for each; Fig. 3, C and D). Therefore, on the basis of the depth-integrated abundances, archaeal *amoA* and *Nitrospina* 16*S* rRNA genes in the upper 150 m at the eddy center ($3.08 \times 10^{10} \pm 0.13 \times 10^{10}$ and $2.60 \times 10^9 \pm 0.22 \times 10^9$ copies m^{-2}) outnumbered those at the edge ($2.20 \times 10^{10} \pm 0.21 \times 10^{10}$ and $4.57 \times 10^8 \pm 0.24 \times 10^8$ copies m^{-2}), with an average increase of 40.1 ± 11.8% and 468.1 ± 53.7%, respectively. When calculating the depth integration of the upper 200 m, the average increases of archaeal *amoA* and *Nitrospina* 16*S* rRNA gene abundances between the eddy center and edge were 8.0 ± 6.5% and 84.1 ± 16.4%, respectively.

DISCUSSION

AOA and NOB show high substrate affinity in the oligotrophic wNPSG

The wNPSG is characterized by permanent thermal stratification of the upper ocean (*17*) that impedes the supply of nutrients from the subsurface, leading to low nutrient concentrations in the euphotic zone. Consistently, NH_4^+ and NO_2^- concentrations were low in our study, which is suggestive of a substrate-limited condition that may cause intense nutrient competition between nitrifiers and phytoplankton. Furthermore, the availability of high light tends to enhance the competitive ability of phytoplankton for nutrients, aggravating substrate limitation of nitrifiers (*23*) and driving their maximum abundance to occur at deeper depths than phytoplankton in the wNPSG vertical profile (Figs. 1E and 3, C and D). Organisms with high substrate affinity would therefore have a competitive advantage in the extremely oligotrophic wNPSG. Here, we report relatively lower K_s values of NH_3 oxidation at 150 to 200 m in the wNPSG eddy system (average, 16.3 ± 15.3 nM) compared with the reported values from other oceanic and coastal areas, including the Sargasso Sea (65 ± 41 nM) (*24*), Hood Canal (98 ± 14 nM) (*25*), the eastern tropical South Pacific (ETSP; 27.2 ± 4.4 nM) (*26*), the South China Sea (49.1 to 167.6 nM) (*27*), the western North Pacific (76 to 247 nM) (*28*, *29*), and the Southern Ocean (28 to 137 nM) (*30*). The K_s values of NO_2^- oxidation (average, 91.0 ± 29.0 nM) were similar to that of the Southern California Bight (70 nM) (*31*), distinctly lower than those reported from the eastern tropical North Pacific (ETNP; 254 ± 161 nM) (*32*) and the Southern Ocean (134 to 403 nM) (*33*), and were at the lower end of reported values from the

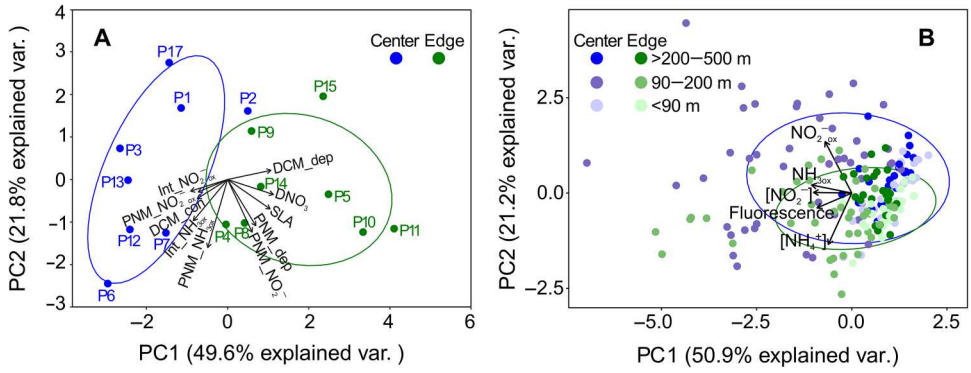

Fig. 4. Principal components analysis (PCA) showing the multivariate variation among all sites or samples in terms of biogeochemical variables. (**A**) PCA results for the first two principal components (PCs) plotted for the depth of the PNM (PNM_dep), NO_2^- concentration in the PNM (PNM_NO_2^-), nitracline depth (DNO_3), DCM depth (DCM_dep), fluorescence value in the DCM (DCM_con), SLA, NH_3 and NO_2^- oxidation rates at the PNM depth (PNM_NH_{3ox} and PNM_$NO_2^-{}_{ox}$, respectively), and integrated NH_{3ox} and $NO_2^-{}_{ox}$ for the upper 150 m (Int_NH_{3ox} and Int_$NO_2^-{}_{ox}$, respectively) across 16 sites. Blue and green dots represent the eddy center and edge sites, respectively. (**B**) PCA results for the first two PCs plotted for NH_{3ox}, $NO_2^-{}_{ox}$, NH_4^+ concentrations, NO_2^- concentrations, and fluorescence values across 192 samples from all depths at the 17 sites. Vectors indicate the direction and strength of each biogeochemical variable to the overall distribution. The percentage of variance explained by each PC is shown in each axis title. The blue and green ellipses represent a normal probability of 0.68 for the datasets from the eddy center and edge sites, respectively.

South China Sea (27 to 506 nM) (*29*) and the subtropical South Atlantic (74 to 167 nM) (*33*). Such low K_s values indicate that nitrifying archaea and bacteria in the wNPSG are highly adapted to the ocean desert. The significantly lower K_s of NH_3 oxidation compared to that of NO_2^- oxidation ($P < 0.05$) in the wNPSG resembles previous studies in the South China Sea (*27*, *29*) and Southern Ocean (*30*, *33*). Moreover, the higher $a°$ value of AOA relative to NOB ($P < 0.05$) suggests a relatively higher affinity of marine AOA toward their substrates. The marine AOA cell size is smaller than marine NOB (*29*, *34*, *35*), thus leading to higher cell surface area to volume ratios, which supports their capability of substrate access under limiting conditions (*9*). The higher substrate affinity of AOA may allow them to draw NH_4^+ concentrations to lower levels than NO_2^- concentrations in the upper 500 m of the wNPSG (Fig. 2, A and B).

We combined the K_s values of marine AOA and NOB from this study with all previously reported K_s values, except those from the ETNP and ETSP where the water column features are greatly different (eutrophic and oxygen deficient). Notably, the K_s values of marine AOA and NOB showed overall exponential decreasing trends from the euphotic zone into the twilight zone (Fig. 5, E and F), indicating an increase in their substrate affinity in extremely substrate-limited environments. Moreover, a lack of light inhibition on nitrifiers at depth provides a favorable condition for improving their substrate affinity (*28*) to cope with energy stress. The detected lowest K_s of AOA at 200 m (8.0 to 11.3 nM) in the wNPSG expands our understanding of their ability to thrive in such an extremely oligotrophic environment. The isopycnal uplift in the cyclonic eddy not only enhances the nutrient supply from the subsurface ocean but also brings planktonic microorganisms from deep into the euphotic zone (*36*). A recent investigation reported a redistribution of nitrifiers driven by a cyclonic eddy in the Gulf of California (*37*). We consistently observed the shallower displacement of AOA and NOB abundance maxima, normally located at the base of or below the euphotic zone (*15*, *38*, *39*), at the eddy center compared with the eddy edge (Fig. 3, C and D). Nevertheless, the nitrifier abundance maxima were located within a similar density range (23.5 to 25 kg m^{-3}; fig. S1) at both the eddy center and edge, which indicates the movement of nitrifiers from subsurface waters into the euphotic zone due to isopycnal uplift. This vertical migration can have a notable impact on the nitrification rate and the distribution of NH_4^+ and NO_2^- in the euphotic zone, as nitrifiers from the subsurface have different kinetic properties from those in the euphotic zone. When deep waters with lower NH_4^+ and NO_2^- concentrations upwell into the euphotic zone, overall concentrations of NH_4^+ and NO_2^- in the euphotic zone become diluted and are more readily used by high-affinity nitrifiers that are also entrained into shallower waters from the deep sea. Although upward migration of nitrifiers may be hindered by light inhibition, the eddy center shows enhanced light attenuation (Fig. 3B), which creates a favorable environment for the high-affinity nitrifiers that upwelled from the subsurface.

Enhanced NH_3 and NO_2^- oxidation in the cyclonic eddy

With the exception of the two edge sites at 150 m, the ambient substrate concentrations were consistently lower than the K_s values, suggesting that nitrification rates were constrained by substrate availability, particularly in the eddy center. Both NH_3 and NO_2^- oxidation rates showed significantly positive correlations with the substrate concentration at the eddy center ($P < 0.01$; Fig. 6A). Similar positive, albeit not always significant, correlations were also found at the eddy edge sites. The slopes of the relationships between NH_3 and NO_2^- oxidation rates and the corresponding substrate concentration reflect the degree of responsiveness of nitrifiers to changes in substrate concentrations. The higher slopes at the eddy center (0.20 and 0.06), despite lower ambient NH_4^+ and NO_2^- concentrations (Fig. 2, A and B), compared to the edge (0.12 and 0.007), suggest a stronger response of nitrifiers to the substrate supply, resulting in elevated nitrification rates at the center. The substrate supply may come from the remineralization of enhanced primary production (further discussed in the next paragraph). The higher abundance of AOA and NOB at the eddy center compared to that at the edge sites, particularly in the euphotic zone (Fig. 3, C and D), may partly explain the elevated slopes (or rates) at the eddy center. Furthermore, it is possible that the high-affinity nitrifiers entrained into upper waters from depth can more completely use substrates,

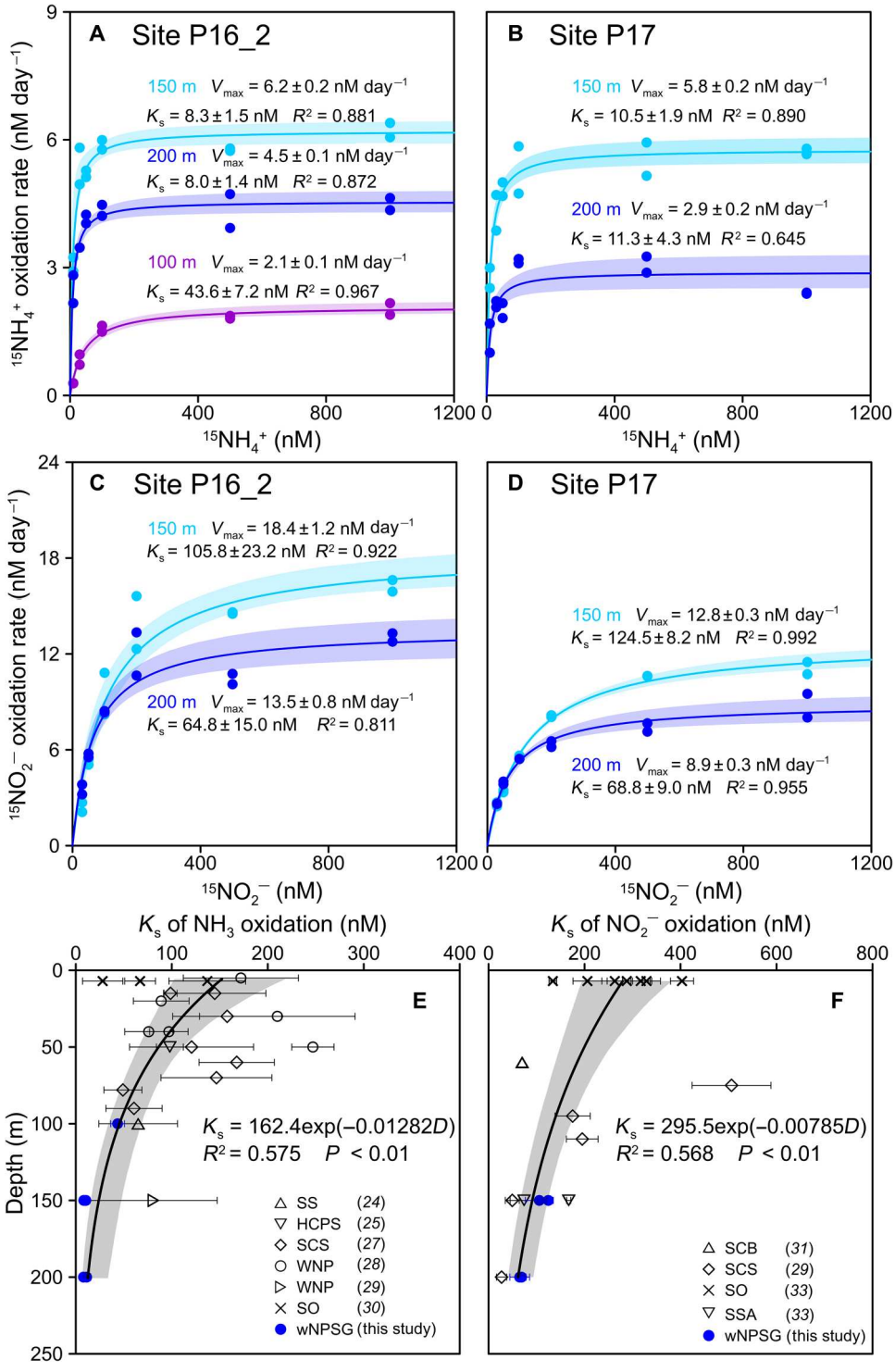

Fig. 5. Michaelis-Menten (M-M) kinetics of NH_3 and NO_2^- oxidation. NH_3 oxidation kinetics at sites (**A**) P16_2 and (**B**) P17; NO_2^- oxidation kinetics at sites (**C**) P16_2 and (**D**) P17. Lines denote the fitting lines of the M-M equation. The best fit for half-saturation constant K_s of (**E**) NH_3 oxidation and (**F**) NO_2^- oxidation against depth. The shaded area represents the 95% confidence interval. Data from this study are shown in blue, and the error bars represent the SEs of the K_s values derived from the M-M equation fit. Data from the literature are shown in black. SS, Sargasso Sea; HCPS, Hood Canal, Puget Sound; SCS, South China Sea; WNP, western North Pacific; SO, Southern Ocean; SCB, Southern California Bight; SSA, subtropical South Atlantic.

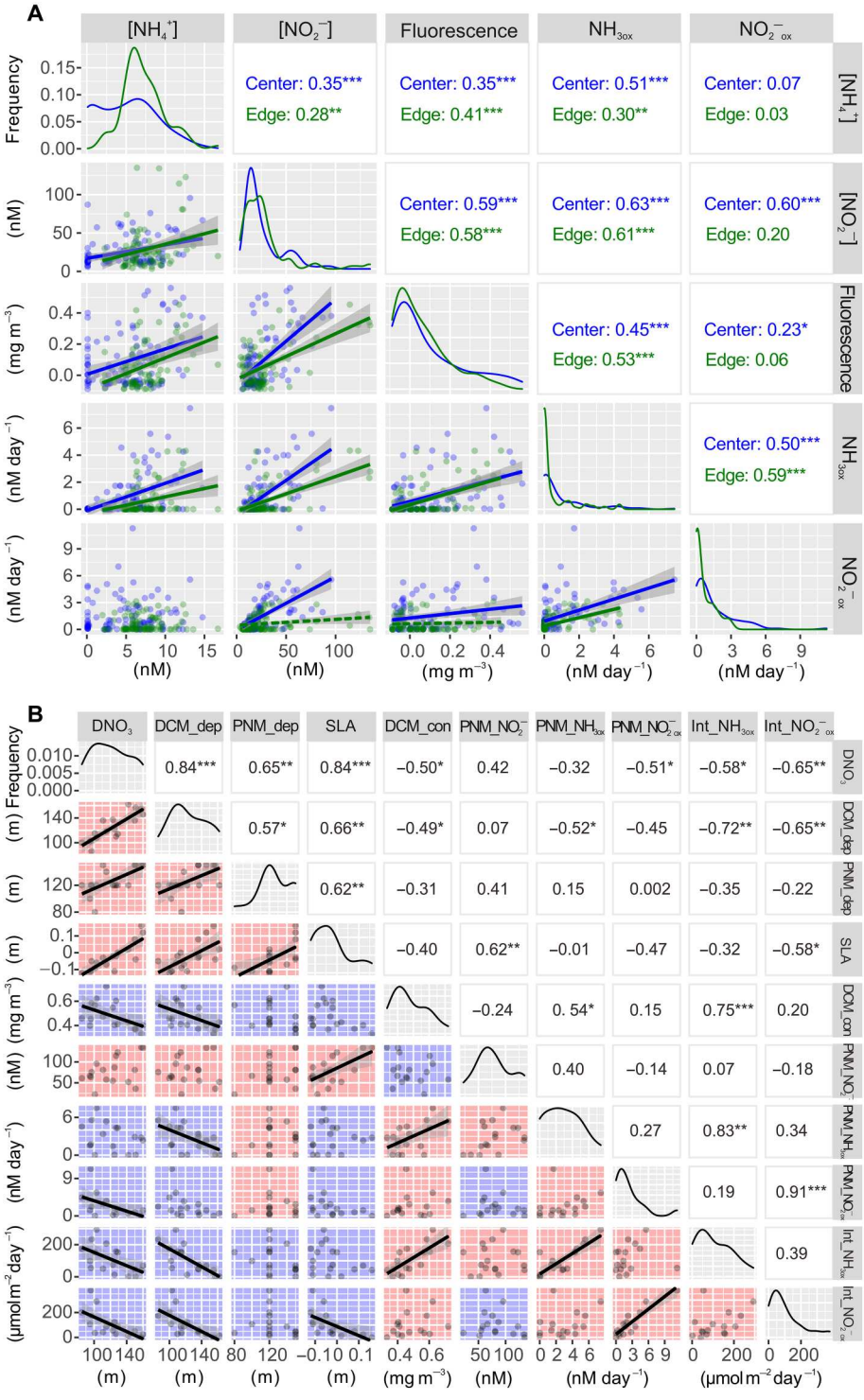

Fig. 6. Pearson correlation analysis among biogeochemical parameters. (**A**) Scatter plot matrix (below the diagonal), histograms (diagonal), and Pearson correlation coefficients (above the diagonal) among NH_3 oxidation rates (NH_{3ox}), NO_2^- oxidation rates ($NO_2^-{}_{ox}$), NH_4^+ concentrations, NO_2^- concentrations, and fluorescence values in 193 samples from all depths at 17 sites. (**B**) Scatter plot matrix (below the diagonal), histograms (diagonal), and Pearson correlation coefficients (above the diagonal) among the PNM depth (PNM_dep), NO_2^- concentrations in the PNM (PNM_NO_2^-), nitracline depth (DNO_3), DCM depth (DCM_dep), fluorescence value in the DCM (DCM_con), SLA, NH_{3ox} and $NO_2^-{}_{ox}$ at the PNM (PNM_NH_{3ox} and PNM_$NO_2^-{}_{ox}$, respectively), and integrated NH_{3ox} and $NO_2^-{}_{ox}$ for the upper 150 m (Int_NH_{3ox} and Int_$NO_2^-{}_{ox}$, respectively) at all 17 sites. Significant correlations are indicated with asterisk (*). *$P < 0.05$; **$P < 0.01$; ***$P < 0.001$. The lines and shadow represent the linear regression line and the 95% confidence interval, respectively. Statistically insignificant correlations are not shown or are represented by dashed lines.

thereby contributing to elevated oxidation rates until a lower ambient concentration is reached at the eddy center.

The NH_3 and NO_2^- oxidation rates also positively correlate with the fluorescence value, with the exception of NO_2^- oxidation at the eddy edge ($P > 0.05$; Fig. 6A). These results suggest that nitrification is regulated by the biological productivity (*9*, *15*), particularly at the eddy center. Upwelled subsurface NO_3^- may stimulate primary productivity, as can be inferred from the synergistic shoaling of the nitracline and DCM [correlation coefficient (r) = 0.84, $P < 0.001$], increase in DCM fluorescence with shoaling of the nitracline ($r = -0.50$, $P < 0.05$) and DCM depth ($r = -0.49$, $P < 0.05$; Fig. 6B), as well as higher NO_3^- assimilation by phytoplankton (table S1; detailed analyses in a separate study) at the eddy center compared to the edge. The supply of reduced nitrogen substrates for nitrification is thus increased by the subsequent remineralization of organic matter (*15*). Moreover, upwelled subsurface NO_3^- may stimulate a transition of phytoplankton community structure from one dominated by prokaryotic cyanobacteria with a high affinity for NH_4^+ to eukaryotes using NO_3^- as the main nitrogen source. These processes may reduce the competition between nitrifiers and phytoplankton for NH_3/NH_4^+ (*8*, *27*, *40*), resulting in higher nitrification activity at the eddy center (Fig. 3, A and B). In addition, a recent study has shown that nitrification was also enhanced in the warm-core anticyclonic eddy center due to a reduced competitive ability of phytoplankton for NH_4^+ in low-light conditions, which may be caused by downwelling. Downwelling mixes phytoplankton and nitrifiers into aphotic waters, reducing nitrifier photo-inhibition and increasing phytoplankton photo-limitation (*41*).

The shoaling of the nitracline promotes the growth and accumulation of phytoplankton (Fig. 1E), which, in turn, enhances light attenuation (Fig. 3B) (*42*). This phenomenon is supported by the observation of concurrent shoaling of the DCM depth, which is an indicator of light attenuation in the euphotic zone (Fig. 6B) (*43*). Enhanced light attenuation further expands the nitrifier niche space (Fig. 3, C and D), which is consistent with higher cell-specific NH_3 and NO_2^- oxidation rates as well as transcript activities of AOA and NOB functional genes ($P < 0.05$ to 0.01) at the eddy center (fig. S2). The increase in niche space and higher nitrifier activity results in a significant correlation between the nitracline depth and observed 150-m integrated rates of NH_3 oxidation ($r = -0.58$, $P < 0.05$) and NO_2^- oxidation ($r = -0.65$, $P < 0.01$) in our study (Fig. 6B). Notably, there is a higher absolute value of the slope (2.93) of the linear relationship for the NO_2^- oxidation than the NH_3 oxidation (|slope| = 2.07), suggesting a greater responsiveness of NO_2^- oxidation to nitracline shoaling. This observation is consistent with the higher percentage increase in the depth-integrated abundances of *Nitrospina* 16*S* rRNA genes than that of the AOA *amoA* genes in the upper 150 m at the eddy center. Because *Nitrospina* is relatively more sensitive to light (*4*, *44*, *45*), its abundance peak is generally located deeper compared to AOA, around the base of the euphotic zone (Fig. 3D) (*29*, *38*, *46*). As a result and in response to upwelling, there is a higher percentage increase in the abundance of NOB compared to AOA within the euphotic zone (Fig. 3C). In addition, the K_s value of NOB decreases more distinctly with depth compared to that of AOA, as indicated by the fitting curves in Fig. 5. Therefore, when deeper-dwelling AOA and NOB upwell and mix with surface AOA and NOB, the NOB population may experience a larger shift in substrate utilization than the AOA population due to larger changes in NOB abundance and K_s values. This speculation could be one of the reasons why the NO_2^- oxidation rates increased more distinctly than NH_3 oxidation rates at the eddy center. Together, these results reveal enhanced NH_3 and NO_2^- oxidation at the eddy center through tightly coupled physical-biological interactions, yet the responses of AOA and NOB are not the same. These different responses may be explained by differences in the traits of these organisms, such as maximum growth rates or population loss rates set by viral lysis or predators. In contrast to a steady-state environment in which nitrification rates are mainly determined by the supply of NH_4^+ from remineralization (*16*), our results imply that, under the influence of cyclonic eddy dynamics, differences in traits between AOA and NOB decouple the two steps of nitrification and affect NO_2^- accumulation in a time-varying state set by eddies.

Reduced concentration of NO_2^- in the PNM of the cyclonic eddy

The typical PNM structure is evident in all sites; however, the PNM at the eddy center is at a shallower depth and contains lower concentrations of NO_2^- compared to the PNM at the edge sites (Fig. 2). Both the PNM depth and concentration were found to have significant and positive correlations with SLA ($r = 0.62$, $P < 0.01$ for each; Fig. 6B), suggesting a notable impact of mesoscale eddy dynamic processes on NO_2^- distribution in the study region. Moreover, the PNM depth shows a significant positive correlation with the nitracline depth ($r = 0.65$, $P < 0.01$; Fig. 6B), indicating that the PNM shoaling at eddy center sites is closely associated with the upward displacement of the nitracline. Upwelling of NO_3^- caused by nitracline shoaling can stimulate phytoplankton growth, which may contribute to the production at the PNM. In addition, a positive correlation between the depths of the PNM and DCM was also observed ($r = 0.57$, $P < 0.05$; Fig. 6B) due to the concurrent shoaling of the DCM associated with enhanced phytoplankton biomass and light attenuation in the cyclonic eddies. Strong correlations of the depth of the PNM with these key water column features have also been found in the ETNP (*47*). Shallowing of the nitracline regulates the substrate supply in the euphotic zone directly through the addition of NO_3^- and indirectly via NH_4^+ regeneration from enhanced remineralization and controls the competition between nitrifiers and phytoplankton for NH_3/NH_4^+ (*27*).

As noted, mesoscale cyclonic eddies enhance NH_3 and NO_2^- oxidation rates overall yet unequally. We observed a negative correlation of the NH_3 oxidation rate at the PNM depth with the depth of the DCM ($r = -0.52$, $P < 0.05$) and a positive correlation with DCM concentrations ($r = 0.54$, $P < 0.05$), indicating the influence of substrate availability on NH_3 oxidation. In contrast, the NO_2^- oxidation rate at the PNM depth was strongly influenced ($r = -0.51$, $P < 0.05$; Fig. 6B) by the nitracline depth that is an indicator directly reflecting the degree of water column stratification affected by the dynamic processes such as upwelling and mixing (*48*). The correlation of NH_3 and NO_2^- oxidation rates with different factors suggests that the second step of nitrification (i.e., NO_2^- oxidation) may be more directly regulated by dynamic processes. Specifically, the displacement of high-affinity deep NOB can cause a more rapidly enhanced NO_2^- oxidation rate in the euphotic zone compared to AOA, which is consistent with the NOB population undergoing a larger shift in abundance and substrate affinity during upwelling. This displacement effect can result in a decoupling between the two steps of nitrification. Thus, NO_2^- concentrations

in the PNM within the eddy systems change due to this decoupling, as reflected by the significant correlation of the PNM NO_2^- concentrations with the difference between inferred NH_3 and NO_2^- oxidation rates (E1: $r = 0.60$, $P < 0.05$; E2: no nitrification rates were determined at the edge despite higher NO_2^- in the PNM; Fig. 7A). The higher inferred rates of NO_2^- oxidation, led by the nitracline shoaling, result in negative net rates of NO_2^- production (Fig. 7B), indicating that the NOB population has the potential to immediately oxidize NO_2^- produced from NH_3 oxidation. It is possible that there is an additional source of NO_2^- from phytoplankton-based processes, but, nevertheless, the negative net rates of NO_2^- production by nitrifiers are closely associated with a reduction in NO_2^- concentration at the PNM in the eddy center (Fig. 7).

The reduced concentration of NO_2^- in the PNM implies an accelerated NO_2^- turnover. In the wNPSG cyclonic eddy system, the average NO_2^- turnover in the PNM by NO_2^- oxidation (calculated as $[NO_2^-]_{avg.}/NO_2^-$ oxidation $rate_{avg.}$) is 17 days at the eddy center and 96 days at the edge, suggesting that mesoscale dynamics accelerate NO_2^- cycling. It has been reported that short-lived (10 to 30 days) and medium (30 days to 1 year) eddies account for 54.7 and 44.9% of the total eddies in the global ocean, respectively (*49*). These findings imply that the lifetime of most eddies is usually longer than the NO_2^- turnover time by NO_2^- oxidation estimated in this study, suggesting that the NO_2^- cycle can maintain a rapid pace within mesoscale eddies. Moreover, sustained NO_2^- cycle activity may be potentially associated with a change in the natural isotopic composition of NO_3^- within mesoscale eddies (*40*). A decreasing trend in the difference between nitrate $\delta^{15}N$ and $\delta^{18}O$ [Δ(15–18)], together with increases in nitrate $\delta^{15}N$ and $\delta^{18}O$ toward the sea surface (fig. S3) clearly suggests the co-occurrence of nitrate assimilation and nitrification in the upper 200 m (*50*–*53*). Newly produced NO_3^- by nitrification introduces a $\delta^{18}O$ value of 1.15 per mil (‰) into the NO_3^- pool (*54*), which is lower than the $\delta^{18}O$ of in situ NO_3^- at 150 to 200 m where nitrate assimilation is limited at our sites. Elevated nitrification rates at 150 to 200 m in the eddy center (Fig. 3, A and B) would be expected to lead to more regenerated NO_3^- with lower $\delta^{18}O$ values, reducing the $\delta^{18}O$ of the in situ NO_3^- pool and thus relatively higher Δ(15–18) values compared to the edge sites, which is what we observed (fig. S3C). Together, these findings demonstrate the notable impacts of mesoscale eddies on the PNM depth, magnitude, and turnover in the oligotrophic ocean, thus improving our understanding of the spatiotemporal variability of the PNM globally.

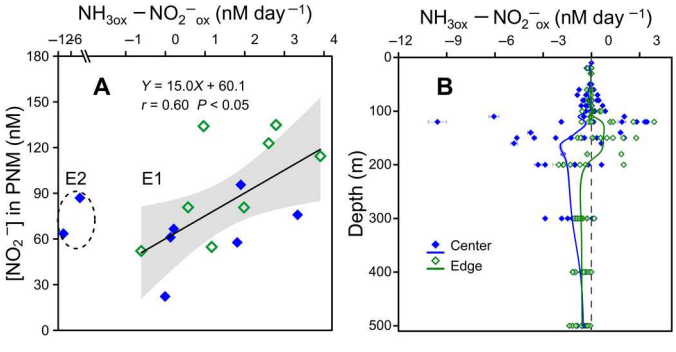

Fig. 7. Differences between NH_3 and NO_2^- oxidation rates. (**A**) Correlation of differences between NH_3 and NO_2^- oxidation rates ($NH_{3ox} - NO_2^-{}_{ox}$) with NO_2^- concentrations in the PNM at each site. The solid black line represents the linear fit for the data from the E1 eddy and the shaded area indicates the 95% confidence interval. The dotted ellipse refers to two sites in the E2 eddy. The blue and green diamonds represent the eddy center and edge, respectively. (**B**) Distributions of $NH_{3ox} - NO_2^-{}_{ox}$ with depth at the eddy center (blue closed diamonds) and edge (green open diamonds). The error bars represent the propagated errors from the SEs of NH_3 and NO_2^- oxidation rates. The blue and green lines represent the average value at the center and edge, respectively. The shaded area indicates the propagated error.

Evaluation of the control of cyclonic eddy on nitrification and PNM

Our measurements of nutrients, rates, and genes allow us to quantitatively estimate the magnitudes of enhancements in NH_3 and NO_2^- oxidation as well as reductions in NO_2^- concentration in the PNM caused by cyclonic eddies. The potential density anomaly at 150 m (base of the euphotic zone) was 23.2 to 24.4 kg m^{-3} at the eddy edge sites, while corresponding densities were observed at depths ranging from 23 to 143 m (average, 97 ± 39 m) at the eddy center sites. These observations indicate that water below the isopycnal surface at an average density of ~23.8 kg m^{-3} upwelled into the euphotic zone at the eddy center while, simultaneously, nitrifiers were entrained from the subsurface into the euphotic zone. Our results show that the integrated abundance of potential subsurface-sourced AOA *amoA* and *Nitrospina* 16*S* rRNA genes from the 23.2 to 24.4 kg m^{-3} isopycnal to 150 m depth accounted for a notable proportion of the total AOA and *Nitrospina* abundances in the euphotic zone of the eddy center sites, when using the eddy edge as a reference (13.7 to 86.4% and 50.9 to 99.8%, respectively). By comparing the average difference of the integrated NH_3 and NO_2^- oxidation rates between the center and edge above 150 m, we estimated that these potential subsurface-sourced nitrifiers contributed approximately 57 and 78% of the gross NH_3 and NO_2^- oxidation, respectively, of the entire euphotic zone (Fig. 8). We acknowledge that using the eddy edge as a reference may have its limitations, given that these locations may experience a deepening of the nutricline and mixed layer, potentially affecting estimates of the contribution of potential subsurface nitrifiers to the NH_3 and NO_2^- oxidation rates at the eddy center. Nevertheless, our findings highlight the role of the eddy-pumping process in driving nitrification in the euphotic zone.

Notably, the average difference between the integrated NH_3 oxidation rate and NO_2^- oxidation rate in the upper 150 m was 36.1 μmol m^{-2} day^{-1} (~95% higher NH_3 oxidation compared to NO_2^- oxidation rates) at the eddy edge sites, suggesting a net production of NO_2^- by nitrification. By contrast, the integrated NO_2^- oxidation rate outpaced the NH_3 oxidation rate by an average of 21.1 μmol m^{-2} day^{-1} (~14% higher NO_2^- oxidation rate) at the eddy center, implying that nitrification acted as a net sink of NO_2^- under the influence of eddy pumping. Thus, we demonstrate a spatial decoupling between nitrification steps caused by eddy perturbations. The enhanced consumption of NO_2^- at the eddy center led to a reduction of ~24 nM in the PNM, accounting for ~36% of the eddy center PNM $[NO_2^-]$ and ~27% of the edge PNM $[NO_2^-]$ during the investigation period (Fig. 8). This finding further suggests an intensification of NO_3^- production via nitrification in the eddy center, which could complicate estimates of NO_3^--based new production in the eddy system (*55*). On the basis of 150-m integrated rates of NO_2^- oxidation and NO_3^- assimilation (table S1), we estimated that nitrification accounted for ~24 and ~17% of the

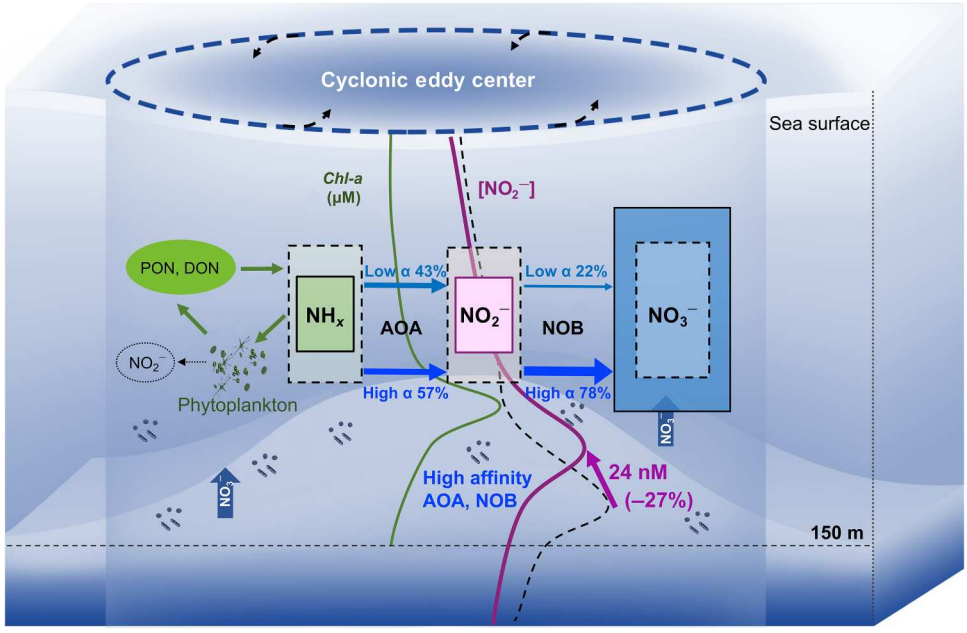

Fig. 8. Schematic depicting effects of mesoscale cyclonic eddies on the two steps of the nitrification pathway, NO_2^- distribution, and PNM in the euphotic zone. In the eddy center (cylinder), the subsurface water mass entraining NO_3^- and high-affinity nitrifiers, AOA and NOB, upwells into the euphotic zone, which stimulates nitrification and accelerates the NO_2^- cycle. The solid and dashed boxes represent the NH_3/NH_4^+, NO_2^-, and NO_3^- reservoirs within and outside the cyclonic eddy, respectively. The bright and dim blue arrows indicate the contribution to the 150-m integrated oxidation rates by high-affinity AOA and NOB in the upwelled subsurface water mass and low-affinity AOA and NOB in the surface water, respectively. The solid green line represents the vertical profile of chlorophyll *a* (*Chl-a*) concentrations within the eddy. The black dashed and pink solid lines represent the vertical profiles of NO_2^- concentrations outside and within the eddy, respectively. The green and black ellipses represent phytoplankton-associated processes. PON, particulate organic nitrogen; DON, dissolved organic nitrogen.

NO_3^- consumed by phytoplankton in the upper 150 m of the eddy center and edge, respectively. These percentages suggest that failure to account for substantial nitrification could lead to a notable overestimation of both new production and carbon export in the eddy system (*55*). On the other hand, when NO_3^- assimilation by phytoplankton is high, active reduction of NO_3^- can potentially release NO_2^-, and NO_2^- uptake may also occur. The net production of NO_2^- resulting from NO_3^- reduction and NO_2^- uptake by phytoplankton may be a noteworthy factor in the formation of the PNM in phytoplankton-rich areas.

In conclusion, we report the most comprehensive investigation of nitrification within wNPSG cyclonic eddies to date and propose a mesoscale mechanism that controls the distribution pattern of the PNM. The eddy-induced uplift of the isopycnal brought NO_3^- from the subsurface into the euphotic zone, potentially supporting phytoplankton primary production. The increased NO_3^- supply, together with increased NH_4^+ caused by organic matter remineralization, reduced NH_3/NH_4^+ competition between phytoplankton and nitrifiers and enhanced nitrification. Along with NO_3^-, nitrifiers with high affinity, indicated by the low K_s values, from the subsurface were also transported into the euphotic zone, where they consumed NH_3/NH_4^+ and NO_2^- until these nutrients reached lower ambient concentrations. Because of relatively larger vertical differences in the abundance and substrate affinity of NOB compared to AOA, we observed more highly enhanced NO_2^- oxidation than NH_3 oxidation, resulting in a switch from net production to net consumption of NO_2^- during nitrification. As a result, NO_2^- turnover was accelerated, and NO_2^- concentrations in the PNM were reduced. This study provides evidence of how mesoscale physical dynamics control the distribution of the PNM in the wNPSG. Our findings suggest that current estimates of new production and carbon export in the ocean, characterized by mesoscale circulation, may be overestimated because of the effects of eddy dynamics on nitrification-dependent PNM distribution. Specifically, when the nitracline is uplifted, it can cause very low PNM NO_2^- concentrations, indicating that nitrification can generate as much NO_3^- as possible from regenerated reduced nitrogen for use in primary production. The increased availability of NO_3^- can thus lead to overestimates of new production. Therefore, it is important to improve parameters of mesoscale circulation in global ocean models to achieve a more comprehensive understanding of biogeochemical cycles in the dynamic ocean.

MATERIALS AND METHODS

Eddy exploration, sampling, and inorganic nitrogen concentrations

Samples were collected, analyzed, and preserved onboard the R/V TAN KAH KEE during a research cruise from 15 March to 20 April 2019 in the wNPSG (Fig. 1). The cruise track crossed several eddies, which were identified and tracked using daily, satellite altimetry–derived SLA from the Copernicus Marine Environmental Monitoring Service (http://marine.copernicus.eu). The centers and edges of these eddies were identified by the sea surface anomaly and horizontal velocity derived in real time from the shipboard acoustic doppler current profiler (WH300 kHz, Teledyne RD Instruments). A total of 17 sites in two eddies (E1 and E2; Fig. 1, A and B) were sampled with a rosette of Niskin bottles attached to a conductivity-

temperature-depth (CTD; Sea-Bird SBE911 plus) profiler. Temperature, salinity, and density were obtained using the CTD system. Fluorescence (mainly from chlorophyll) values and PAR were detected using an ECO-FLNTU fluorometer (WET Labs) and QCP2300-HP sensor (Biospherical Instruments), respectively, attached to the CTD profiler. The bottom of the euphotic zone was defined as 0.1% of surface PAR.

Water samples for inorganic nitrogen analysis were collected in triplicate in 125 ml of acid-washed, high-density polyethylene (HDPE) bottles. The ultra-trace NH_4^+ concentrations were analyzed onboard immediately after collection using the fluorometric *o*-phthaldialdehyde method by a sensitive flow-batch system, coupling fluorescence detection with flow analysis and solid-phase extraction (*56*). The detection limit of our batch analyses was 1.3 nM based on three times the SD (0.44) of the blank measurements (n = 7). Samples for NO_2^- and NO_3^- concentrations were frozen at −20°C until analysis in the laboratory. NO_3^- concentrations were measured using the colorimetric method with a Technicon AutoAnalyzer III (AA3, Bran+Luebbe); the detection limit was 70 nM, and the precision was better than 1% (*57*). NO_2^- concentrations, along with NO_3^- concentrations near or below the detection limit of the AA3, were determined using the flow injection analysis–liquid waveguide capillary cell method, which has a detection limit of 5 nM and precision better than 3.1% (*58*).

Incubation experiments for NH_3 and NO_2^- oxidation rates and kinetics

To determine the instantaneous rates of NH_3 and NO_2^- oxidation at all 17 sites (Fig. 1, A and B), approximately 250 ml of seawater in duplicate was incubated in acid-cleaned Nalgene HDPE bottles after ^{15}N-labeled NH_4^+ (^{15}N-NH_4^+) or ^{15}N-labeled NO_2^- (^{15}N-NO_2^-) tracer (98% of ^{15}N atom, Sigma-Aldrich) was added (final concentration of 30 nM). To alleviate the loss of ^{15}N by phytoplankton uptake and improve accuracy for samples from the upper 100 to 120 m, additional ^{14}N-NO_2^- and ^{14}N-NO_3^- (final concentration of 0.8 μM) was added to the incubations for NH_3 and NO_2^- oxidation, respectively. After the tracers were added and mixed, 30 ml of *seawater* was immediately filtered through a 0.2-μm syringe and used to determine the initial isotopic values. The Nalgene bottles, containing the remaining seawater, were incubated in the dark for 11 to 24 hours and 11 to 60 hours at near in situ temperature (±1°C) to determine the NH_3 and NO_2^- oxidation rates, respectively. After incubation, approximately 30 ml of seawater was filtered through a 0.2-μm syringe into a 50-ml centrifuge tube and stored at −20°C until analysis.

NH_3 and NO_2^- oxidation kinetic experiments were performed at 100, 150, and 200 m at sites P16_1 and P17 (Fig. 1). The dependence of the NH_3 or NO_2^- oxidation rate on substrate concentrations was investigated using six different concentrations of ^{15}N-NH_4^+ (0.01, 0.03, 0.05, 0.1, 0.5, and 1 μM) or ^{15}N-NO_2^- (0.03, 0.05, 0.1, 0.2, 0.5, and 1 μM). For each set, a tracer was added separately into duplicate 250-ml Nalgene HDPE bottles. After adding the tracer and mixing, 30 ml of sample was immediately filtered through a 0.2-μm syringe filter to measure the initial isotopic values ($t0$). Dark, 24 hours of incubations or time-course [23 ($t1$) hours and 55 ($t2$) hours] incubations were performed in a thermostat incubator at *in situ* temperature (±1°C) for NH_3 or NO_2^- oxidation rates, respectively. Incubations were terminated by filtering approximately 30 ml of seawater through a 0.2-μm syringe filter. The potential ^{14}N dilution effect caused by NH_4^+ regeneration in our incubation experiments was low, based on the significant linear relationships between ^{15}N concentrations in products and incubation time (P < 0.01 to 0.05; fig. S4). Nevertheless, the relative regeneration rate of NH_4^+ to the NH_3 oxidation rate should be considered when interpreting our results. It is possible that the rapid cycling of NH_4^+ in the subtropical gyre may have had an impact on our measurements, and additional investigations are needed to evaluate this potential influence.

Isotope measurements and rate calculations

The δ^{15}N value of NO_x^- (δ^{15}N-NO_x^-) was measured using the denitrifier method for determining the NH_3 oxidation rate (*59*, *60*). Briefly, NO_x^- was first quantitatively converted to N_2O using the bacterial strain *Pseudomonas aureofaciens* (American Type Culture Collection, no. 13985); the δ^{15}N values of N_2O were then measured using a Thermo Finnigan Gasbench–coupled isotope ratio mass spectrometer (GC-IRMS, Thermo Delta V Advantage). Three NO_3^- international reference materials (USGS 34, IAEA-N3, and USGS 32) were used to calibrate the measured δ^{15}N-NO_x^-. At an injection level of 20 nmol N, the accuracy of the analysis of these standards was better than 0.2‰. For determining the NO_2^- oxidation rate, samples were first treated with sulfamic acid (≥99%, Sigma-Aldrich) for 12 hours at room temperature (22°C to 26°C) in the dark to remove NO_2^- (*61*) and then neutralized with sodium hydroxide. The δ^{15}N value of NO_3^- (δ^{15}N-NO_3^-) was determined by the denitrifier method as described above.

The rates of NH_3 and NO_2^- oxidation were determined on the basis of the accumulation of ^{15}N in the product pool relative to the initial. In the incubations for NH_3 oxidation in the upper 100 m and incubations for NO_2^- oxidation at all depths, the final concentrations of NH_3 and NO_2^- were close to or less than the measured or reported K_s of NH_3 and NO_2^- oxidation (Fig. 5, E and F). We therefore applied a linear regression approach using Eqs. 1 and 2 to estimate the ^{14}N-reaction rates (*8*, *26*).

$$R_{\text{bulk}} = \frac{[S] \times (r_t - r_0)}{t \times f^{15}} \quad (1)$$

$$R_{14\text{N}} = R_{\text{bulk}} \times \frac{[S_i]}{[S_i] + [S_t]} \quad (2)$$

where R_{bulk} is the reaction rate (nanomolar per day) under the bulk substrate concentration (ambient substrate + tracer); S denotes the product concentration (nanomolar); f^{15} is the fraction of added ^{15}N tracer to the total substrate concentration at the beginning of the incubation, r_t and r_0 are ^{15}N% of the product pool at the end and beginning of the incubation, respectively; and t is the incubation duration (hours). $R_{14\text{N}}$ is the ^{14}N-reaction rate calibrated by linear interpolation, and S_i and S_t are the initial substrate and final tracer concentrations, respectively.

Below 100 m, the final concentrations of NH_4^+ were 2.2 to 4.5 times higher than the K_s [8.0 to 11.3 nM; average, 9.5 ± 1.3 (propagated error) nM] of NH_3 oxidation, measured at 150 and 200 m at sites P16_2 and P17 (Fig. 5, A and B). A NH_4^+ concentration higher than K_s precluded the application of the linear first-order model for deriving the ^{14}N-reaction rate. Therefore, we derived the ^{14}N-NH_3

oxidation rates below 100 m using the M-M equation

$$V_{14N} = \frac{V_{max} \times [S_i]}{K_s + [S_i]} \quad (3)$$

where V_{14N} is the ^{14}N-NH_3 oxidation rate, $[S_i]$ is the in situ NH_4^+ concentration, K_s was assigned as 9.5 ± 1.3 nM (i.e., the average K_s values at 150 and 200 m), and V_{max} is the potential maximum rate. V_{max} was derived using Eq. 4 deformed from the M-M equation

$$V_{max} = \frac{(K_s + S) \times V_{bulk}}{S} \quad (4)$$

where S is bulk NH_4^+ concentration (ambient substrate + tracer) in the incubation systems, V_{bulk} is the bulk reaction rates (obtained from Eq. 1), and K_s was assigned as 9.5 ± 1.3 nM. The propagated error is shown in data S1.

The rates of NH_3 and NO_2^- oxidation in the kinetics experiments were calculated as the accumulation rates of ^{15}N atoms in the production pool (R_{15}) using Eq. 5

$$R_{15} = \frac{[S] \times (r_t - r_0)}{t} \quad (5)$$

where S denotes the product concentrations in the incubation, and r_t and r_0 are the ^{15}N fractions of the product pool at the end and beginning of the incubation, respectively. These ^{15}N accumulation rates and ^{15}N concentrations were fitted using the M-M equation in SigmaPlot 12.5 software to obtain the kinetic constants (V_{max} and K_s).

DNA extraction and quantitative PCR amplification

For DNA extraction, 2 liters of seawater was filtered through 0.2-μm–pore size polycarbonate membranes (25 mm diameter; Millipore) under gentle peristaltic pressure. All membranes were flash-frozen in liquid nitrogen and stored at −80°C until analysis. DNA was extracted using the phenol-chloroform-isoamyl alcohol method as described by Nercessian *et al.* (*62*). The concentration and purity of the genomic DNA were checked with a NanoDrop spectrophotometer (Thermo Fisher Scientific 2000/2000c). Abundances of the archaeal *amoA* and *Nitrospina* 16*S* rRNA genes were quantified in triplicate using the quantitative polymerase chain reaction (qPCR) method with a CFX 96 real-time system (Bio-Rad). Standard curves were constructed using serial dilutions (10^0 to 10^7 copies/μl) of quantified, linearized plasmid-containing target gene sequences. The qPCR primers, reaction mixtures, and thermocycling conditions are listed in table S2. We used two primer pairs to quantify the high-ammonia concentration cluster and the low-ammonia concentration cluster of AOA (table S2). The total archaeal *amoA* gene abundance was calculated as the sum of archaeal *amoA* gene abundances yielded with the two primer sets (*63*). The efficiencies of the qPCR amplification ranged from 90 to 102% with coefficient of determination (R^2) > 0.99. The specificity of the qPCR reactions was checked by melting curve analysis and agarose gel electrophoresis. The uncertain products were further sequenced to confirm their veracity. In addition, qPCR was conducted to examine the abundance of the β-proteobacterial *amoA* gene with the primer set amoA-1F and amoA-2R (*64*). AOB were detected only in two samples (10^2 copies liter^{-1}) among all DNA samples.

Statistical analysis

Because a normal distribution of an individual dataset was not always produced, the difference between two independent datasets and paired datasets was tested using the nonparametric Mann-Whitney *U* test and Wilcoxon signed-rank test, respectively, with SPSS 20.0 software. PCA was performed using the *Z*-transformed biogeochemical parameters and visualized by ggbiplot packages in R. Pearson correlation coefficients among biogeochemical parameters were calculated and visualized by GGally packages in R.

Supplementary Materials

This PDF file includes:
Materials and Methods
Figs. S1 to S4
Tables S1 and S2
Legend for data S1
References

Other Supplementary Material for this manuscript includes the following:
Data S1

REFERENCES AND NOTES

1. J. E. Dore, D. M. Karl, Nitrite distributions and dynamics at Station ALOHA. *Deep Sea Res. Part II Top. Stud. Oceanogr.* **43**, 385–402 (1996).
2. N. Gruber, The marine nitrogen cycle: Overview and challenges, in *Nitrogen in the Marine Environment* (Academic, ed. 2, 2008), pp. 1–50.
3. R. J. Olson, Differential photoinhibition of marine nitrifying bacteria: A possible mechanism for the formation of the primary nitrite maximum. *J. Mar. Res.* **39**, 227–238 (1981).
4. B. Ward, R. J. Olson, M. J. Perry, Microbial nitrification rates in the primary nitrite maximum off southern California. *Deep Sea Res. Part I Oceanogr. Res. Pap.* **29**, 247–255 (1982).
5. C. Buchwald, K. L. Casciotti, Isotopic ratios of nitrite as tracers of the sources and age of oceanic nitrite. *Nat. Geosci.* **6**, 308–313 (2013).
6. Y. Chen, P. Bardhan, X. Zhao, M. Zheng, Y. Qiu, M. Chen, Nitrite cycle indicated by dual isotopes in the northern South China Sea. *J. Geophys. Res. Biogeosci.* **126**, e2020JG006129 (2021).
7. A. E. Santoro, C. M. Sakamoto, J. M. Smith, J. N. Plant, A. L. Gehman, A. Z. Worden, K. S. Johnson, C. A. Francis, K. L. Casciotti, Measurements of nitrite production in and around the primary nitrite maximum in the central California Current. *Biogeosciences* **10**, 7395–7410 (2013).
8. X. S. Wan, H. X. Sheng, M. Dai, M. J. Church, W. Zou, X. Li, D. A. Hutchins, B. B. Ward, S. J. Kao, Phytoplankton-nitrifier interactions control the geographic distribution of nitrite in the upper ocean. *Global Biogeochem. Cycles* **35**, e2021GB007072 (2021).
9. E. J. Zakem, A. Al-Haj, M. J. Church, G. L. van Dijken, S. Dutkiewicz, S. Q. Foster, R. W. Fulweiler, M. M. Mills, M. J. Follows, Ecological control of nitrite in the upper ocean. *Nat. Commun.* **9**, 1206 (2018).
10. D. Tilman, *Resource Competition and Community Structure*, Monographs in Population Biology (Princeton Univ. Press, 1982).
11. M. W. Lomas, F. Lipschultz, Forming the primary nitrite maximum: Nitrifiers or phytoplankton? *Limnol. Oceanogr.* **51**, 2453–2467 (2006).
12. S. Haas, B. M. Robicheau, S. Rakshit, J. Tolman, C. K. Algar, J. LaRoche, D. W. Wallace, Physical mixing in coastal waters controls and decouples nitrification via biomass dilution. *Proc. Natl. Acad. Sci. U.S.A.* **118**, e2004877118 (2021).
13. C. M. Moore, M. M. Mills, K. R. Arrigo, I. Berman-Frank, L. Bopp, P. W. Boyd, E. D. Galbraith, R. J. Geider, C. Guieu, S. L. Jaccard, T. D. Jickells, J. La Roche, T. M. Lenton, N. M. Mahowald, E. Maranon, I. Marinov, J. K. Moore, T. Nakatsuka, A. Oschlies, M. A. Saito, T. F. Thingstad, A. Tsuda, O. Ulloa, Processes and patterns of oceanic nutrient limitation. *Nat. Geosci.* **6**, 701–710 (2013).
14. A. Olsen, R. M. Key, S. van Heuven, S. K. Lauvset, A. Velo, X. Lin, C. Schirnick, A. Kozyr, T. Tanhua, M. Hoppema, S. Jutterstrom, R. Steinfeldt, E. Jeansson, M. Ishii, F. F. Perez, T. Suzuki, The global ocean data analysis project version 2 (GLODAPv2)–An internally consistent data product for the world ocean. *Earth Syst. Sci. Data* **8**, 297–323 (2016).
15. T. Shiozaki, M. Ijichi, K. Isobe, F. Hashihama, K.-i. Nakamura, M. Ehama, K.-i. Hayashizaki, K. Takahashi, K. Hamasaki, K. Furuya, Nitrification and its influence on biogeochemical cycles from the equatorial Pacific to the Arctic Ocean. *ISME J.* **10**, 2184–2197 (2016).

16. E. J. Zakem, B. Bayer, W. Qin, A. E. Santoro, Y. Zhang, N. M. Levine, Controls on the relative abundances and rates of nitrifying microorganisms in the ocean. *Biogeosciences* **19**, 5401–5418 (2022).
17. D. M. Karl, Minireviews: A sea of change: Biogeochemical variability in the North Pacific Subtropical Gyre. *Ecosystems* **2**, 181–214 (1999).
18. B. Qiu, S. Chen, P. Klein, H. Sasaki, Y. Sasai, Seasonal mesoscale and submesoscale eddy variability along the North Pacific Subtropical Countercurrent. *J. Phys. Oceanogr.* **44**, 3079–3098 (2014).
19. W. Cui, W. Wang, J. Zhang, J. Yang, Identification and census statistics of multicore eddies based on sea surface height data in global oceans. *Acta Oceanol. Sin.* **39**, 41–51 (2020).
20. P. Xiu, F. Chai, Eddies affect subsurface phytoplankton and oxygen distributions in the North Pacific Subtropical Gyre. *Geophys. Res. Lett.* **47**, e2020GL087037 (2020).
21. P. Klein, G. Lapeyre, The oceanic vertical pump induced by mesoscale and submesoscale turbulence. *Annu. Rev. Mar. Sci.* **1**, 351–375 (2009).
22. R. Le Borgne, R. T. Barber, T. Delcroix, H. Y. Inoue, D. J. Mackey, M. Rodier, Pacific warm pool and divergence: Temporal and zonal variations on the equator and their effects on the biological pump. *Deep Sea Res. Part II Top. Stud. Oceanogr.* **49**, 2471–2512 (2002).
23. M. Mdutyana, S. J. Thomalla, R. Philibert, B. B. Ward, S. E. Fawcett, The seasonal cycle of nitrogen uptake and nitrification in the Atlantic Sector of the Southern Ocean. *Global Biogeochem. Cycles* **34**, e2019GB006363 (2020).
24. S. E. Newell, S. E. Fawcett, B. B. Ward, Depth distribution of ammonia oxidation rates and ammonia-oxidizer community composition in the Sargasso Sea. *Limnol. Oceanogr.* **58**, 1491–1500 (2013).
25. R. E. A. Horak, W. Qin, A. J. Schauer, E. V. Armbrust, A. E. Ingalls, J. W. Moffett, D. A. Stahl, A. H. Devol, Ammonia oxidation kinetics and temperature sensitivity of a natural marine community dominated by Archaea. *ISME J.* **7**, 2023–2033 (2013).
26. X. Peng, C. A. Fuchsman, A. Jayakumar, M. J. Warner, A. H. Devol, B. B. Ward, Revisiting nitrification in the Eastern Tropical South Pacific: A focus on controls. *J. Geophys. Res. Oceans* **121**, 1667–1684 (2016).
27. X. S. Wan, H.-X. Sheng, M. Dai, Y. Zhang, D. Shi, T. W. Trull, Y. Zhu, M. W. Lomas, S.-J. Kao, Ambient nitrate switches the ammonium consumption pathway in the euphotic ocean. *Nat. Commun.* **9**, 915 (2018).
28. M. N. Xu, X. Li, D. Shi, Y. Zhang, M. Dai, T. Huang, P. M. Glibert, S. J. Kao, Coupled effect of substrate and light on assimilation and oxidation of regenerated nitrogen in the euphotic ocean. *Limnol. Oceanogr.* **64**, 1270–1283 (2019).
29. Y. Zhang, W. Qin, L. Hou, E. J. Zakem, X. Wan, Z. Zhao, L. Liu, K. A. Hunt, N. Jiao, S.-J. Kao, K. Tang, X. Xie, J. Shen, Y. Li, M. Chen, X. Dai, C. Liu, W. Deng, M. Dai, A. E. Ingalls, D. A. Stahl, G. J. Herndl, Nitrifier adaptation to low energy flux controls inventory of reduced nitrogen in the dark ocean. *Proc. Natl. Acad. Sci. U.S.A.* **117**, 4823–4830 (2020).
30. M. Mdutyana, X. Sun, J. M. Burger, R. F. Flynn, S. Smith, N. R. Horsten, A. N. Roychoudhury, H. Planquette, E. Bucciarelli, S. J. Thomalla, B. B. Ward, S. E. Fawcett, The kinetics of ammonium uptake and oxidation across the Southern Ocean. *Limnol. Oceanogr.* **67**, 973–991 (2022).
31. R. J. Olson, ^{15}N tracer studies of the primary nitrite maximum. *J. Mar. Res.* **39**, 203–226 (1981).
32. X. Sun, Q. Ji, A. Jayakumar, B. B. Ward, Dependence of nitrite oxidation on nitrite and oxygen in low oxygen seawater. *Geophys. Res. Lett.* **44**, 7883–7891 (2017).
33. M. Mdutyana, T. Marshall, X. Sun, J. M. Burger, S. J. Thomalla, B. B. Ward, S. E. Fawcett, Controls on nitrite oxidation in the upper Southern Ocean: Insights from winter kinetics experiments in the Indian sector. *Biogeosciences* **19**, 3425–3444 (2022).
34. E. Spieck, S. Keuter, T. Wenzel, E. Bock, W. Ludwig, Characterization of a new marine nitrite oxidizing bacterium, *Nitrospina watsonii* sp nov., a member of the newly proposed phylum "*Nitrospinae*". *Syst. Appl. Microbiol.* **37**, 170–176 (2014).
35. M. G. Pachiadaki, E. Sintes, K. Bergauer, J. M. Brown, N. R. Record, B. K. Swan, M. E. Mathyer, S. J. Hallam, P. Lopez-Garcia, Y. Takaki, T. Nunoura, T. Woyke, G. J. Herndl, R. Stepanauskas, Major role of nitrite-oxidizing bacteria in dark ocean carbon fixation. *Science* **358**, 1046–1051 (2017).
36. C. E. Nelson, C. A. Carlson, C. S. Ewart, E. R. Halewood, Community differentiation and population enrichment of Sargasso Sea bacterioplankton in the euphotic zone of a mesoscale mode-water eddy. *Environ. Microbiol.* **16**, 871–887 (2014).
37. R. Ramos-de la Cruz, S. Pajares, M. Merino-Ibarra, M. A. Monreal-Gómez, E. Coria-Monter, Distribution of nitrogen-cycling genes in an oxygen-depleted cyclonic eddy in the Alfonso Basin, Gulf of California. *Mar. Freshwater Res.* **72**, 1173–1184 (2021).
38. J. M. Beman, B. N. Popp, S. E. Alford, Quantification of ammonia oxidation rates and ammonia-oxidizing archaea and bacteria at high resolution in the Gulf of California and eastern tropical North Pacific Ocean. *Limnol. Oceanogr.* **57**, 711–726 (2012).
39. A. E. Santoro, K. L. Casciotti, C. A. Francis, Activity, abundance and diversity of nitrifying archaea and bacteria in the central California Current. *Environ. Microbiol.* **12**, 1989–2006 (2010).
40. S. E. Fawcett, M. W. Lomas, J. R. Casey, B. B. Ward, D. M. Sigman, Assimilation of upwelled nitrate by small eukaryotes in the Sargasso Sea. *Nat. Geosci.* **4**, 717–722 (2011).
41. S. Wallschuss, M. Mdutyana, R. G. Parrott, H. J. Forrer, R. Roman, D. R. Walker, I. J. Ansorge, S. E. Fawcett, The influence of Agulhas leakage on primary production and nitrogen cycling in the Southeastern Atlantic Ocean. *J. Geophys. Res. Oceans* **127**, e2022JC018971 (2022).
42. D. J. McGillicuddy Jr., A. R. Robinson, D. A. Siegel, H. W. Jannasch, R. Johnson, T. D. Dickey, J. Mcneil, A. F. Michaels, A. H. Knap, Influence of mesoscale eddies on new production in the Sargasso Sea. *Nature* **394**, 263–266 (1998).
43. M. Cornec, H. Claustre, A. Mignot, L. Guidi, L. Lacour, A. Poteau, F. D'Ortenzio, B. Gentili, C. Schmechtig, Deep chlorophyll maxima in the global ocean: Occurrences, drivers and characteristics. *Global Biogeochem. Cycles* **35**, e2020GB006759 (2021).
44. M. A. Guerrero, R. D. Jones, Photoinhibition of marine nitrifying bacteria. II. Dark recovery after monochromatic or polychromatic irradiation. *Mar. Ecol. Prog. Ser.* **141**, 193–198 (1996).
45. S. G. Horrigan, A. F. Carlucci, P. M. Williams, Light inhibition of nitrification in sea-surface films. *J. Mar. Res.* **39**, 557–565 (1981).
46. J. M. Beman, J. Leilei Shih, B. N. Popp, Nitrite oxidation in the upper water column and oxygen minimum zone of the eastern tropical North Pacific Ocean. *ISME J.* **7**, 2192–2205 (2013).
47. N. M. Travis, C. L. Kelly, M. R. Mulholland, K. L. Casciotti, Nitrite cycling in the primary nitrite maxima of the eastern tropical North Pacific. *Biogeosciences* **20**, 325–347 (2023).
48. P. Cermeno, S. Dutkiewicz, R. P. Harris, M. Follows, O. Schofield, P. G. Falkowski, The role of nutricline depth in regulating the ocean carbon cycle. *Proc. Natl. Acad. Sci. U.S.A.* **105**, 20344–20349 (2008).
49. G. Chen, G. Han, Contrasting short-lived with long-lived mesoscale eddies in the global ocean. *J. Geophys. Res. Oceans* **124**, 3149–3167 (2019).
50. S. E. Fawcett, B. B. Ward, M. W. Lomas, D. M. Sigman, Vertical decoupling of nitrate assimilation and nitrification in the Sargasso Sea. *Deep Sea Res. Part I* **103**, 64–72 (2015).
51. J. Y. T. Yang, J. M. Tang, S. Kang, M. Dai, S. J. Kao, X. Yan, M. N. Xu, C. Du, Comparison of nitrate isotopes between the South China Sea and Western North Pacific Ocean: Insights into biogeochemical signals and water exchange. *J. Geophys. Res. Oceans* **127**, e2021JC018304 (2022).
52. F. Deman, D. Fonseca-Batista, A. Roukaerts, M. I. García-Ibáñez, E. Le Roy, E. P. D. N. Thilakarathne, M. Elskens, F. Dehairs, F. Fripiat, Nitrate supply routes and impact of internal cycling in the North Atlantic Ocean inferred from nitrate isotopic composition. *Global Biogeochem. Cycles* **35**, e2020GB006887 (2021).
53. T. A. Marshall, D. M. Sigman, L. M. Beal, A. Foreman, A. Martínez-García, S. Blain, E. Campbell, F. Fripiat, R. Granger, E. Harris, G. H. Haug, D. Marconi, S. Oleynik, P. A. Rafter, R. Roman, K. Sinyanya, S. M. Smart, S. E. Fawcett, The Agulhas Current transports signals of local and remote Indian Ocean nitrogen cycling. *J. Geophys. Res. Oceans* **128**, e2022JC019413 (2023).
54. D. M. Sigman, P. J. DiFiore, M. P. Hain, C. Deutsch, Y. Wang, D. M. Karl, A. N. Knapp, M. F. Lehmann, S. Pantoja, The dual isotopes of deep nitrate as a constraint on the cycle and budget of oceanic fixed nitrogen. *Deep Sea Res. Part I* **56**, 1419–1439 (2009).
55. A. Yool, A. P. Martin, C. Fernández, D. R. Clark, The significance of nitrification for oceanic new production. *Nature* **447**, 999–1002 (2007).
56. Y. Zhu, D. Yuan, Y. Huang, J. Ma, S. Feng, A sensitive flow-batch system for on board determination of ultra-trace ammonium in seawater: Method development and shipboard application. *Anal. Chim. Acta* **794**, 47–54 (2013).
57. M. Dai, L. Wang, X. Guo, W. Zhai, Q. Li, B. He, S.-J. Kao, Nitrification and inorganic nitrogen distribution in a large perturbed river/estuarine system: The Pearl River Estuary, China. *Biogeosciences* **5**, 1227–1244 (2008).
58. J.-Z. Zhang, Shipboard automated determination of trace concentrations of nitrite and nitrate in oligotrophic water by gas-segmented continuous flow analysis with a liquid waveguide capillary flow cell. *Deep Sea Res., Part I* **47**, 1157–1171 (2000).
59. D. M. Sigman, K. L. Casciotti, M. Andreani, C. Barford, M. Galanter, J. K. Böhlke, A bacterial method for the nitrogen isotopic analysis of nitrate in seawater and freshwater. *Anal. Chem.* **73**, 4145–4153 (2001).
60. K. L. Casciotti, D. M. Sigman, M. G. Hastings, J. K. Böhlke, A. Hilkert, Measurement of the oxygen isotopic composition of nitrate in seawater and freshwater using the denitrifier method. *Anal. Chem.* **74**, 4905–4912 (2002).
61. J. Granger, D. M. Sigman, Removal of nitrite with sulfamic acid for nitrate N and O isotope analysis with the denitrifier method. *Rapid Commun. Mass Spectrom.* **23**, 3753–3762 (2009).
62. O. Nercessian, E. Noyes, M. G. Kalyuzhnaya, M. E. Lidstrom, L. Chistoserdova, Bacterial populations active in metabolism of C_1 compounds in the sediment of Lake Washington, a freshwater lake. *Appl. Environ. Microb.* **71**, 6885–6899 (2005).

63. K. Bergauer, E. Sintes, J. van Bleijswijk, H. Witte, G. J. Herndl, Abundance and distribution of archaeal acetyl-CoA/propionyl-CoA carboxylase genes indicative for putatively chemoautotrophic Archaea in the tropical Atlantic's interior. *FEMS Microbiol. Ecol.* **84**, 461–473 (2013).
64. T. J. Mincer, M. J. Church, L. T. Taylor, C. Preston, D. M. Karl, E. F. DeLong, Quantitative distribution of presumptive archaeal and bacterial nitrifiers in Monterey Bay and the North Pacific Subtropical Gyre. *Environ. Microbiol.* **9**, 1162–1175 (2007).
65. C. Wuchter, B. Abbas, M. J. Coolen, L. Herfort, J. van Bleijswijk, P. Timmers, M. Strous, E. Teira, G. J. Herndl, J. J. Middelburg, S. Schouten, J. S. Sinninghe Damsté, Archaeal nitrification in the ocean. *Proc. Natl. Acad. Sci. U.S.A.* **103**, 12317–12322 (2006).
66. E. Sintes, K. Bergauer, D. De Corte, T. Yokokawa, G. J. Herndl, Archaeal *amo*A gene diversity points to distinct biogeography of ammonia-oxidizing *Crenarchaeota* in the ocean. *Environ. Microbiol.* **15**, 1647–1658 (2013).
67. S. Rani, H.-W. Koh, S.-K. Rhee, H. Fujitani, S.-J. Park, Detection and diversity of the nitrite oxidoreductase Alpha subunit (*nxrA*) gene of *Nitrospina* in marine sediments. *Microb. Ecol.* **73**, 111–122 (2017).

Acknowledgments: We thank all crew members of R/V TAN KAH KEE for assistance in sampling, T. Huang for the onboard measurement of NH_4^+, R. Du and J. Ni for assistance with RNA extraction, and W. Shi for assistance with MATLAB software. We also thank Q. Chen, M. Du, Y. Zhu, J. Shen, and P. Cai for help during the manuscript preparation, as well as S. Kender for editing the English text of a draft of this manuscript. **Funding:** This work was funded by the NSFC projects (42125603, 41730533, 92251303, and 42188102). **Author contributions:** Y.Z. and M.D. conceived and designed the research. L.L. performed nitrification experiments. L.L., Y.Z., M.C., X.S.W., C.D., E.J.Z., and W.Q. analyzed data. Z.L., Z.H., Z.-P.J., K.Z., and H.L. performed physical dynamics measurements and analysis and provided the SLA and CTD data. H.S. and S.-J. K. performed nitrate assimilation experiments. J.-Y.T.Y. and X.L. performed natural isotopic composition analyses. M.C., D.Z., L.Y., and L.H. performed DNA/RNA extraction and qPCR analyses. Y.Z., L.L., M.C., and X.S.W. wrote the paper. All authors discussed the results and contributed to the final version of the paper. **Competing interests:** The authors declare that they have no competing interests. **Data and materials availability:** All data needed to evaluate the conclusions in the paper are present in the paper and/or the Supplementary Materials.

Submitted 2 August 2022
Accepted 17 July 2023
Published 16 August 2023
10.1126/sciadv.ade2078

ScienceAdvances

Reduced nitrite accumulation at the primary nitrite maximum in the cyclonic eddies in the western North Pacific subtropical gyre

Li Liu, Mingming Chen, Xianhui S. Wan, Chuanjun Du, Zhiyu Liu, Zhendong Hu, Zong-Pei Jiang, Kuanbo Zhou, Hongyang Lin, Hui Shen, Duo Zhao, Lanying Yuan, Lei Hou, Jin-Yu T. Yang, Xiaolin Li, Shuh-Ji Kao, Emily J. Zakem, Wei Qin, Minhan Dai, and Yao Zhang

Sci. Adv. **9** (33), eade2078. DOI: 10.1126/sciadv.ade2078